

Communication

# Enhanced Photocatalytic Removal of Hexavalent Chromium over Bi<sub>12</sub>TiO<sub>20</sub>/RGO Polyhedral Microstructure Photocatalysts

Huihui Gan \*, Shuo Pan, Xiuhang Liu and Ying Huang

Civil and Environmental Engineering Department, Ningbo University, Ningbo 315100, China; panshuo86@163.com (S.P.); liuxiuhang7@163.com (X.L.); huangying1@nbu.edu.cn (Y.H.)

\* Correspondence: ganhuihui@nbu.edu.cn; Tel.: +86-574-8760-5196

**Abstract:** A Bi<sub>12</sub>TiO<sub>20</sub>/RGO photocatalyst with polyhedron microstructure was fabricated via the template-free hydrothermal method, and the visible-light-induced photocatalytic activity of the prepared Bi<sub>12</sub>TiO<sub>20</sub> was also evaluated by the photocatalytic reduction of heavy metal pollutants. The structures and optical properties of the prepared Bi<sub>12</sub>TiO<sub>20</sub>/RGO were characterized by X-ray diffraction (XRD), scanning electron microscopy (SEM), and UV-vis diffuse reflectance spectrum (UV-vis DRS). The effects of the reaction time and mineralizer concentration on the formation of the Bi<sub>12</sub>TiO<sub>20</sub> polyhedral microstructure were analyzed. The enhanced photocatalytic performances of Bi<sub>12</sub>TiO<sub>20</sub>/RGO were observed which were ascribed to the combination of the Bi<sub>12</sub>TiO<sub>20</sub> microstructure induced photogenerated charges and the RGO nanostructure as a photogenerated charges carrier. The effect of organic acids, p-hydroxybenzoic acid (PHBA), chloroacetic acid, and citric acid on the Cr(VI) photocatalytic reduction was also discussed. This work provides an insight into the design of the bismuth-based microstructure photocatalyst towards the application for environment purification of heavy metals.

**Keywords:** bismuth titanate; reduced graphene oxide; photocatalytic; heavy metal pollutants



**Citation:** Gan, H.; Pan, S.; Liu, X.; Huang, Y. Enhanced Photocatalytic Removal of Hexavalent Chromium over Bi<sub>12</sub>TiO<sub>20</sub>/RGO Polyhedral Microstructure Photocatalysts. *Nanomaterials* **2022**, *12*, 2138. <https://doi.org/10.3390/nano12132138>

Academic Editor: Marco Stoller

Received: 30 May 2022

Accepted: 17 June 2022

Published: 22 June 2022

**Publisher's Note:** MDPI stays neutral with regard to jurisdictional claims in published maps and institutional affiliations.



**Copyright:** © 2022 by the authors. Licensee MDPI, Basel, Switzerland. This article is an open access article distributed under the terms and conditions of the Creative Commons Attribution (CC BY) license (<https://creativecommons.org/licenses/by/4.0/>).

## 1. Introduction

Chromium is essential in many industrial activities, such as leather tanning, dyeing, glass, galvanic industries, and ceramics; however, it results in hexavalent chromium species in the wastewater. Unlike most organic pollutants, the heavy metal chromium is not biodegradable and its high mobility and toxicity in water pose a threat to the environment. Chromium existing as a hexavalent in water is listed as a priority pollutant in many countries due to its carcinogenic and mutagenic effect [1,2]. The traditional treatment methods, including adsorption, membrane filtration, biological treatment, chemical precipitation, and electrochemical reduction still have many drawbacks, such as having high energy consumption and being time-consuming [3]. Compared with Cr(VI), Cr(III) is much less toxic and mobile in water. Thus, the remediation reduction of Cr(VI) to Cr(III) has gained considerable attention. Recently, photocatalysis driven by solar energy for reducing Cr(VI) to Cr(III) has been the focus of numerous studies [4–8]. TiO<sub>2</sub>-WO<sub>3</sub>-PANI membranes were designed to realize the effective reduction of chromium (VI) in a reactor under visible light [9]. BiSI nanorods with rich sulfur vacancies were reported to be favorable for Cr(VI) adsorption and showed excellent photocatalytic Cr(VI) reduction ability [10]. In these methods, the photocatalytic reduction of Cr(VI) happens based on the photo-excited electron from the conduction band of photocatalysts or the generated reactive radical during the process under UV or visible light.

Bismuth-based materials have been considered as one of the alternative photocatalysts to TiO<sub>2</sub> because of their unique electronic structures and visible-light response. Among bismuth oxides semiconductors, bismuth titanate Bi<sub>12</sub>TiO<sub>20</sub> with its unique sillenite structure is a promising photocatalyst for the removal of organic pollutants owing to the excellent

chemical stability, layered structure, and narrow optical bandgap. Moreover, it has been found that the properties of the photocatalysts can be further enhanced by controlling the synthesis of crystals with a fabricated morphology and an exposed highly active crystal facets [11,12]. Nanowires  $\text{Bi}_{12}\text{TiO}_{20}$  were synthesized using titanium isopropoxide (TTIP) as starting materials and polyvinyl alcohol (PVA) as a surfactant, which displayed significantly improved activity for the photocatalytic decomposition of methyl orange under UV-light irradiation [13]. Flower-like  $\text{Bi}_{12}\text{TiO}_{20}$  prepared by solvothermal treatment with TTIP was reported to fabricate  $\text{Bi}_{12}\text{TiO}_{20}$ -graphene nanoarchitectures and exhibited excellent photocatalytic activity for the degradation of methyl orange (MO) and p-nitrophenol (PNP) under simulated sunlight [14]. The  $\text{Bi}_{12}\text{TiO}_{20}$  micro-tetrahedrons exposed by {111} facets coupled with g- $\text{C}_3\text{N}_4$  showed higher visible-light photocatalytic activity for degradation of gaseous formaldehyde [15]. Based on the above consideration, the fabrication of the  $\text{Bi}_{12}\text{TiO}_{20}$  microstructure presents great appeal and expectation for promoting their photoreduction ability for Cr(VI).

Constructing an efficient photoinduced charge transfer interface is also critical for the higher efficient photocatalysts. Reduced graphene oxide (RGO) has been extensively researched and it has been clearly evidenced that assembling and decorating carbon nanosheets with the semiconductor can promote the photocatalytic and photoelectrochemical processes [16–19]. Therefore, introducing a small amount of RGO into the  $\text{Bi}_{12}\text{TiO}_{20}$  microstructure could form an efficient path for charge carrier migration to improve the photocatalytic ability.

In this work,  $\text{Bi}_{12}\text{TiO}_{20}$ /RGO microstructures were fabricated through free-template and one-step hydrothermal synthesis by introducing reduced graphene oxide (RGO) on the polyhedral microstructure  $\text{Bi}_{12}\text{TiO}_{20}$ . The physical and optical properties of  $\text{Bi}_{12}\text{TiO}_{20}$ /RGO were analyzed by various characterizations. The effects of the reaction time and mineralizer on the formation of the  $\text{Bi}_{12}\text{TiO}_{20}$  polyhedral microstructure were also investigated. The photocatalytic properties of  $\text{Bi}_{12}\text{TiO}_{20}$ /RGO for reducing Cr(VI) in the presence and absence of organic acid compounds were also discussed.

## 2. Material and Methods

### 2.1. Synthesis of Catalyst

The  $\text{Bi}_{12}\text{TiO}_{20}$ /RGO polyhedral microstructure was prepared by a hydrothermal method. Typically, a certain amount of graphene oxide (GO) was dispersed in 2 mol/L NaOH solution under sonication for 20 min, and then  $\text{Bi}_2\text{O}_3$  and  $\text{TiO}_2$  with a mole ratio of  $[\text{Bi}]/[\text{Ti}] = 12:1$  were added into the solution while it was continuously ultrasonically dispersed for 10 min. The theoretical mass ratio of  $\text{Bi}_{12}\text{TiO}_{20}$  and GO was 1:0.01. After that, 80 mL of the mixture solution was transferred into a 100 mL Teflon-lined stainless-steel autoclave and hydrothermally reacted for 24 h at 220 °C. The obtained precipitate was washed several times until the pH attained neutral and the as-prepared sample was dried in an oven at 80 °C for 12 h. As references, the pure  $\text{Bi}_{12}\text{TiO}_{20}$  was also prepared under the method similar to those above without added graphene oxide.

### 2.2. Characterization

Powder X-ray diffraction (XRD) patterns of the samples were characterized on a D8 Advance X-ray diffractometer (Bruker AXS, Karlsruhe, Germany) with Cu  $K\alpha$  radiation. The morphologies of the powders were analyzed by a Phenom Pro scanning electron microscope (Phenom Pro, Eindhoven, The Netherlands). The UV-vis spectra were measured by a Lambda 950 UV/vis/NIR spectrometer (Perkin Elmer, Waltham, MA, USA). The Fourier IR spectroscopy was performed by using a Nicolet-670 Fourier transform infrared spectrometer (ThermoFisher, Carlsbad, CA, USA).

### 2.3. Photocatalytic Activity

The photocatalytic activities of catalysts were evaluated under visible light Xenon lamp (PLS-SXE300(BF), Beijing, China) with a 400 nm cut-off filter ( $\lambda \geq 400$  nm). In a typical

process, the Cr(VI) solution (50  $\mu\text{mol/L}$ ) was adjusted to pH 3.0 by nitric acid solution, and a 0.15 g sample was added to 100 mL Cr(VI) solution. To ensure the adsorption–desorption equilibrium between Cr(VI) and catalysts, the suspension was stirred in the dark for 120 min. After attaining equilibrium, a definite time interval under the illumination of visible light, the aliquots samples were taken out of the reaction suspensions. The reductive rate of Cr(VI) was detected by the diphenylcarbazide method at 540 nm with a UV-2550 UV–vis spectrophotometer. Further, to explore the effect of various organic acids on the Cr(VI) reduction, p-hydroxybenzoic acid (PHBA), chloroacetic acid, and citric acid, with a concentration of 0.1  $\mu\text{mol/L}$ , were added to the Cr(VI) solution, respectively.

### 3. Results and Discussion

#### 3.1. Composition and Morphology

The phase and crystal structure of  $\text{Bi}_{12}\text{TiO}_{20}/\text{RGO}$  was analyzed by XRD. As shown in Figure 1, all diffraction peaks of the prepared  $\text{Bi}_{12}\text{TiO}_{20}/\text{RGO}$  samples could be well indexed to the cubic  $\text{Bi}_{12}\text{TiO}_{20}$  (JCPDS No. 34-0097), which indicated that the crystal structure of  $\text{Bi}_{12}\text{TiO}_{20}$  was stable for the fabrication of hybrid composites. The strong and sharp diffraction peaks indicated that  $\text{Bi}_{12}\text{TiO}_{20}$  had good crystallinity in the composites. The XRD patterns for the RGO were not observed in  $\text{Bi}_{12}\text{TiO}_{20}/\text{RGO}$ , which is mainly because of the relatively low content level of RGO, as well as the RGO sheets being further exfoliated during hydrothermal treatment [8,20].

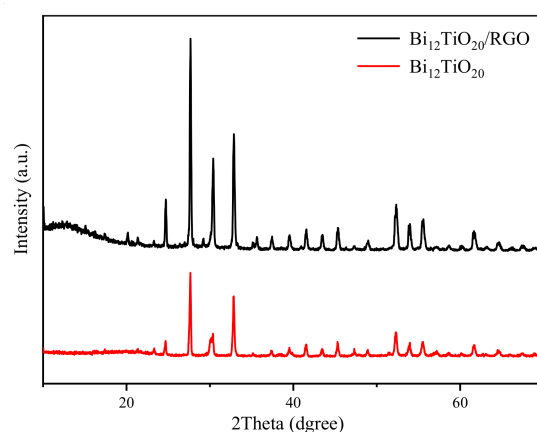


**Figure 1.** XRD patterns of the  $\text{Bi}_{12}\text{TiO}_{20}/\text{RGO}$  polyhedral microstructure and pure  $\text{Bi}_{12}\text{TiO}_{20}$ .

In order to detect the structure of the samples,  $\text{Bi}_{12}\text{TiO}_{20}$  and  $\text{Bi}_{12}\text{TiO}_{20}/\text{RGO}$  were analyzed by FT-IR spectrum. As displayed in Figure 2, for pure  $\text{Bi}_{12}\text{TiO}_{20}$ , five peaks were shown at  $459\text{ cm}^{-1}$ ,  $524\text{ cm}^{-1}$ ,  $576\text{ cm}^{-1}$ ,  $662\text{ cm}^{-1}$ , and  $828\text{ cm}^{-1}$ , respectively. These peaks all contributed to Bi–O vibration modes; this result was consistent with the characteristic peaks of sillenite. Because of the introduction of RGO, more peaks appeared in the  $\text{Bi}_{12}\text{TiO}_{20}/\text{RGO}$  samples. The peak located at  $1634\text{ cm}^{-1}$  corresponded to stretching vibration modes of aromatic C=C bonds which are the basic unit of reduced graphene oxide. Moreover, the peak at  $3450\text{ cm}^{-1}$  was attributed to hydroxyl (–OH) groups from the absorbed water and the residual of the reduced graphene oxide. Generally, these results revealed that  $\text{Bi}_{12}\text{TiO}_{20}$  and  $\text{Bi}_{12}\text{TiO}_{20}/\text{RGO}$  were synthesized successfully.

Figure 3 shows the Raman spectra of  $\text{Bi}_{12}\text{TiO}_{20}$  and  $\text{Bi}_{12}\text{TiO}_{20}/\text{RGO}$ . The curves for  $\text{Bi}_{12}\text{TiO}_{20}$  at  $100\text{ cm}^{-1}$  versus  $900\text{ cm}^{-1}$  are similar to previously reported data [21,22]. Specifically, the peaks at  $204$  and  $262\text{ cm}^{-1}$  arose due to Bi–O bending and stretching vibrations and O–Ti–O bending vibrations, respectively. The peaks at  $324$  and  $535\text{ cm}^{-1}$  were attributed to the O–O bonding vibrations in  $\text{Bi}_{12}\text{TiO}_{20}$ . The peaks at  $716$  and  $850\text{ cm}^{-1}$  were attributed to the symmetric and antisymmetric stretching of the  $\text{TiO}_4$  tetrahedra, respectively [21,23].

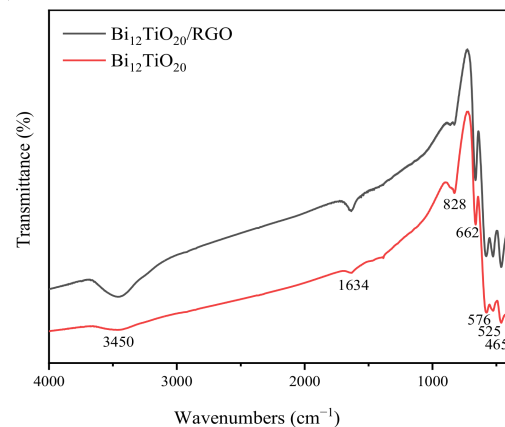


**Figure 2.** FT-IR spectra of  $\text{Bi}_{12}\text{TiO}_{20}/\text{RGO}$  and pure  $\text{Bi}_{12}\text{TiO}_{20}$  Morphology analysis.

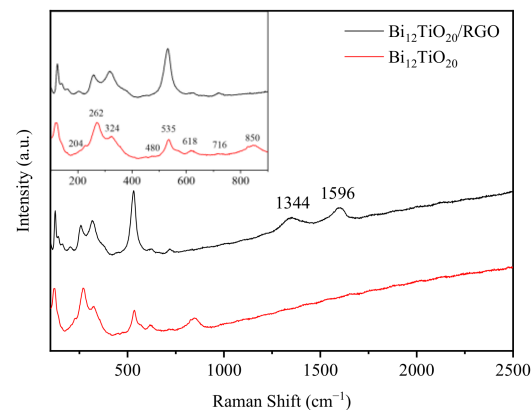


**Figure 3.** Raman spectra of  $\text{Bi}_{12}\text{TiO}_{20}/\text{RGO}$  and pure  $\text{Bi}_{12}\text{TiO}_{20}$ .

The  $\text{Bi}_{12}\text{TiO}_{20}/\text{RGO}$  composite had essentially the same peaks as  $\text{Bi}_{12}\text{TiO}_{20}$ , except that it showed strong characteristic peaks in the Raman spectra at  $1344$  and  $1596\text{ cm}^{-1}$ , corresponding to the D and G bands of RGO, respectively [8,24], which indicated successful introduction of RGO. Both the D and G bands are characteristic peaks in the Raman spectra of different defects scattered by carbon atoms. The intensity ratio ( $I_{\text{D}}/I_{\text{G}}$ ) of the D and G peaks can be used to assess the defect density of the carbon material [25,26]. A value of 0.89 for  $I_{\text{D}}/I_{\text{G}}$  in  $\text{Bi}_{12}\text{TiO}_{20}/\text{RGO}$  indicated the presence of exact crystal structure defects in  $\text{Bi}_{12}\text{TiO}_{20}/\text{RGO}$  [27], resulting in easier transport of photogenerated carriers in graphene and thus a lower probability of photoelectron-hole complexation.

The morphologies of pure  $\text{Bi}_{12}\text{TiO}_{20}$  at different hydrothermal times were observed in Figure 4a–d. It can be seen that, after the hydrothermal reaction for 1 h to 2 h, the  $\text{Bi}_{12}\text{TiO}_{20}$  formed a mainly tetrahedral structure, and when the reaction time was increased to 6 h, the polyhedral microstructure appeared. With a 24 h reaction time,  $\text{Bi}_{12}\text{TiO}_{20}$  mainly existed with a polyhedral microstructure. In addition to the hydrothermal time, the  $\text{OH}^-$  ions also played an important part in the morphology formation in the hydrothermal process [15,28]. As shown in Figure 4e,f, with 1 mol/L NaOH solution, the  $\text{Bi}_{12}\text{TiO}_{20}$  showed a tetrahedral structure and non-uniform polyhedral microstructure. When the  $\text{OH}^-$  ions increased to 4 mol/L, the  $\text{Bi}_{12}\text{TiO}_{20}$  can be described as a uniform polyhedral microstructure. According to relevant literature descriptions [15], the influence of  $\text{OH}^-$  anions on specific surfaces may affect the crystal growth direction and rate, which may be the cause of a uniform polyhedral microstructure. Therefore, the reaction time and the  $\text{OH}^-$  ions are key factors for controlling the development of the  $\text{Bi}_{12}\text{TiO}_{20}$  polyhedral microstructure (Figure 4i). The morphologies of  $\text{Bi}_{12}\text{TiO}_{20}/\text{RGO}$  are shown in Figure 5. It can be seen that the  $\text{Bi}_{12}\text{TiO}_{20}/\text{RGO}$  still exhibited a polyhedral microstructure after the introduction of RGO and RGO had no effect on crystal surface growth. The small size and

polyhedral microstructure will enhance light reflection and absorption, further contributing to the photocatalytic degradation effect.

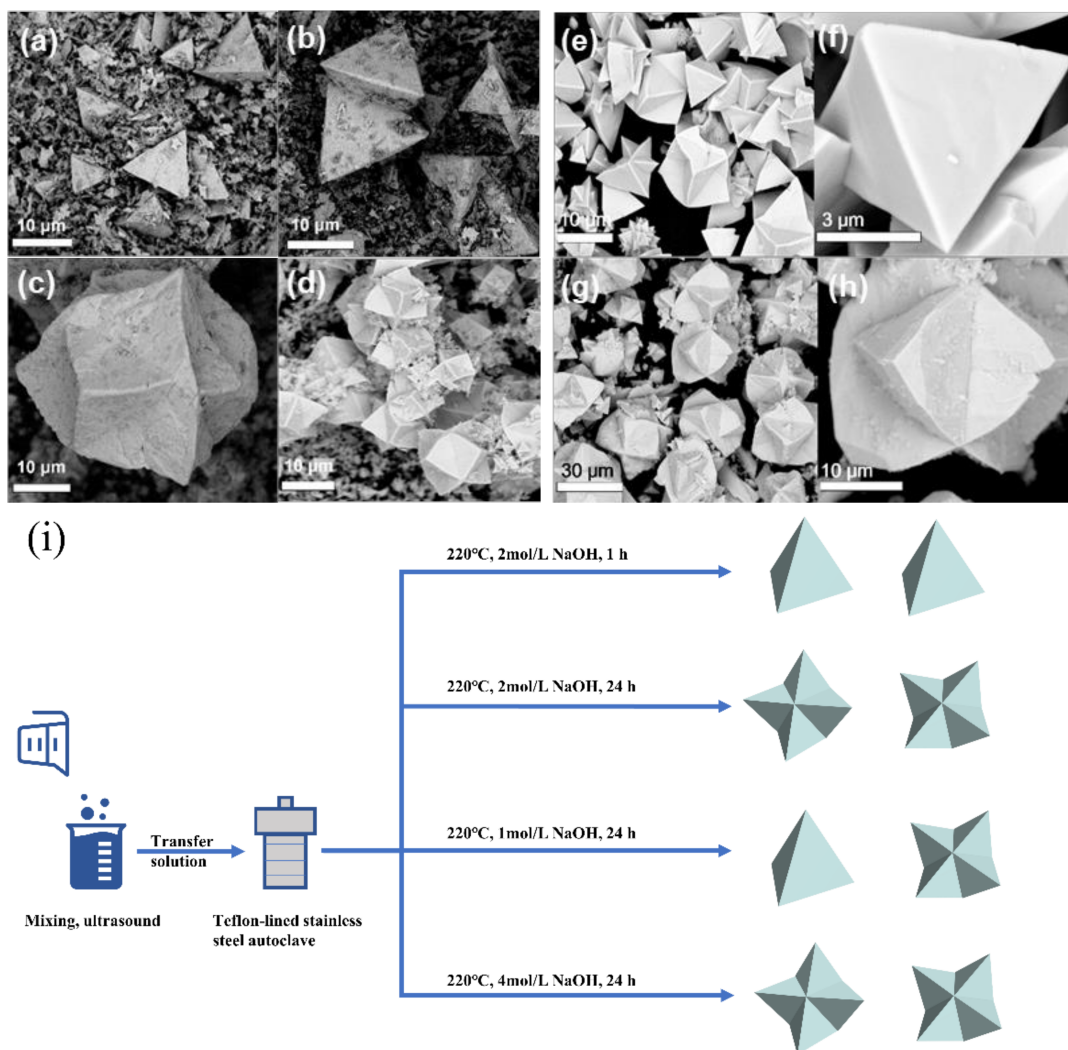


**Figure 4.** SEM images of the  $\text{Bi}_{12}\text{TiO}_{20}$  synthesized at different times, 1 h (a), 2 h (b), 6 h (c), 24 h (d); and with different NaOH concentrations, 1 mol/L (e,f), 4 mol/L (g,h), Growth mechanism of  $\text{Bi}_{12}\text{TiO}_{20}$  under different conditions (i).

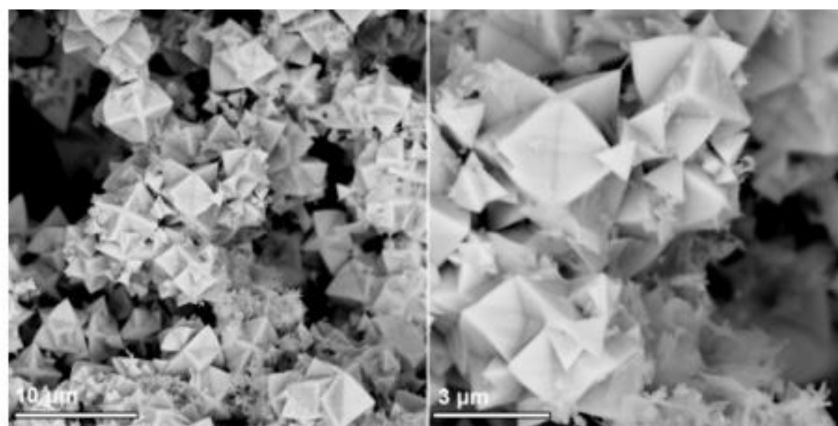


**Figure 5.** SEM images of the  $\text{Bi}_{12}\text{TiO}_{20}/\text{RGO}$  samples.

The UV–vis diffuse reflectance was conducted to evaluate the optical properties of each as-prepared sample. As shown in Figure 6a, pure  $\text{Bi}_{12}\text{TiO}_{20}$  exhibited a photo-absorption from UV to visible light region, and its absorption onset was around 459 nm. Due to the background absorption of the reduced graphene, it was obvious that the absorbance intensities of  $\text{Bi}_{12}\text{TiO}_{20}/\text{RGO}$  strengthened in the range from 400 nm to 700 nm. On the other hand, there was a red shift in the absorbance onset from 459 to 503 nm due to the carbon modification of  $\text{Bi}_{12}\text{TiO}_{20}$ . As a result, the visible utilization of  $\text{Bi}_{12}\text{TiO}_{20}/\text{RGO}$  composites was enhanced. As shown in Figure 6b, After calculation [29],  $E_g$  values of  $\text{Bi}_{12}\text{TiO}_{20}/\text{RGO}$  and pure  $\text{Bi}_{12}\text{TiO}_{20}$  were 2.95 eV and 3.10 eV, respectively. The  $E_g$  of the carbon-modified  $\text{Bi}_{12}\text{TiO}_{20}$  became smaller, further demonstrating the enhanced utilization of visible light by  $\text{Bi}_{12}\text{TiO}_{20}/\text{RGO}$ .

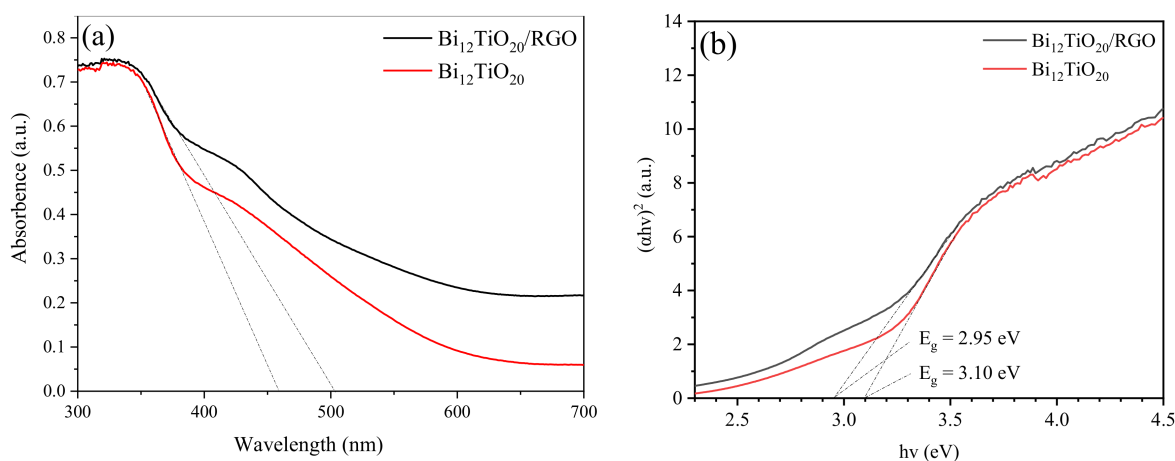


**Figure 6.** UV–vis diffuse reflectance spectra (a,b) Tauc plots of the  $\text{Bi}_{12}\text{TiO}_{20}/\text{RGO}$  and pure  $\text{Bi}_{12}\text{TiO}_{20}$ .

### 3.2. Photocatalytic Reduction of Hexavalent Chromium under Visible Light

The photocatalytic reduction ability of Cr(VI) using  $\text{Bi}_{12}\text{TiO}_{20}$  and  $\text{Bi}_{12}\text{TiO}_{20}/\text{RGO}$  were evaluated. Before irradiation, the adsorption of Cr(VI) in solution of the samples was in equilibrium after 120 min, and the adsorption removal was 13.8% and 22.6% for pure  $\text{Bi}_{12}\text{TiO}_{20}$  and  $\text{Bi}_{12}\text{TiO}_{20}/\text{RGO}$ , respectively (In Figure 7b).  $\text{Bi}_{12}\text{TiO}_{20}/\text{RGO}$  showed better adsorption for the removal of Cr(VI) than pure  $\text{Bi}_{12}\text{TiO}_{20}$ . As shown in Figure 7, within 180 min visible light irradiation, the removal rate of Cr(VI) by pure  $\text{Bi}_{12}\text{TiO}_{20}$  was just 64.1%, while the removal rate of the  $\text{Bi}_{12}\text{TiO}_{20}/\text{RGO}$  reached 82.7%. Additionally, according to the equation of the pseudo-first-order kinetics model:  $-\ln(C/C_0) = kt$ , where  $C_0$  is the initial concentration for each pollutant,  $C$  is the instantaneous concentration at the irradiating time of  $t$ , and  $k$  is the first-order rate constant for degradation. The corresponding reaction rate constants were calculated to be  $0.0085 \text{ min}^{-1}$  and  $0.0060 \text{ min}^{-1}$  for  $\text{Bi}_{12}\text{TiO}_{20}/\text{RGO}$  and  $\text{Bi}_{12}\text{TiO}_{20}$ , respectively. There is some literature on the reduction removal of Cr(VI) by designing a photocatalysis system and limited reports using  $\text{Bi}_{12}\text{TiO}_{20}$  photocatalyst. The  $\text{TiO}_2\text{-WO}_3$  incorporated PANI membrane showed 98.50% removal of Cr(VI) by filtration and 67.32% by photocatalytic reduction [9]. The Biochar/Bi/ $\text{Fe}_3\text{O}_4$  composites presented 95% adsorption-photocatalytic removal for Cr(VI) in 180 min under visible light irradiation [30]. By using the graphene-based composite ((BOCI/CNCl/rGH), the removal efficiencies reached 87% and 85% in a tetracycline hydrochloride and Cr(VI) coexistence system, higher than those in a TCH or Cr(VI) alone system [31]. Compared with the reported literature, the  $\text{Bi}_{12}\text{TiO}_{20}/\text{RGO}$  polyhedral microstructure exhibited great potential for the visible-light photoreduction removal system of Cr(VI). With the introduction of RGO, the  $\text{Bi}_{12}\text{TiO}_{20}/\text{RGO}$  exhibited both better adsorptive and photocatalytic ability.

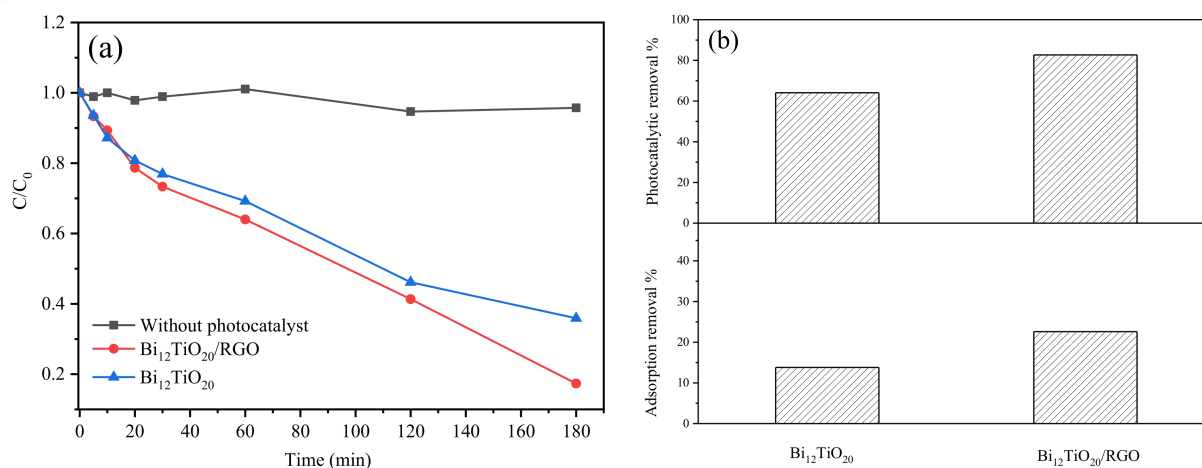


**Figure 7.** (a)  $C/C_0$  vs. time plot for the photocatalytic reduction of Cr(VI) by the Bi<sub>12</sub>TiO<sub>20</sub>/RGO and pure Bi<sub>12</sub>TiO<sub>20</sub>; (b) The photocatalytic removal and adsorption removal of Cr(VI) by the Bi<sub>12</sub>TiO<sub>20</sub>/RGO and pure Bi<sub>12</sub>TiO<sub>20</sub>.

Furthermore, different organic acids, PHBA, chloroacetic acid, and citric acid were added to explore the photocatalytic reduction of Cr(VI) by Bi<sub>12</sub>TiO<sub>20</sub>/RGO. Generally speaking, the addition of organics are beneficial for the photocatalytic reduction of Cr(VI) by improving the separation of photogenerated charge via the scavenging of holes in the photocatalytic reactions [32,33]. As shown in Figure 8a,b, with the addition of PHBA, there was an obvious acceleration of the Cr(VI) photocatalytic removal. Under 180 min visible light irradiation with the addition of PHBA, the degradation rate increased by 3.4% and the kinetic constant increased from 0.0089 min<sup>-1</sup> to 0.011 min<sup>-1</sup>. While for Cr(VI), the photocatalytic removal was not obviously improved with the addition of chloroacetic acid, and even decrease with citric acid, and the kinetic constant decreased from 0.0089 min<sup>-1</sup> to 0.0051 min<sup>-1</sup>. It might be because of the competitive adsorption between organic acid and Cr(VI). From Figure 8c, the Cr(VI) adsorption depressed with the addition of PHBA, chloroacetic acid, and citric acid, and the adsorption removal was significantly decreased with citric acid. The result indicated that the Cr(VI) adsorption could largely influence the photocatalytic reduction reaction in the Cr(VI) and organic acid combined pollutants.

### 3.3. Catalytic Mechanism

A possible mechanism for the photocatalytic reduction of Cr(VI) by Bi<sub>12</sub>TiO<sub>20</sub>/RGO polyhedral microstructure composites can be interpreted. Generally, an increased adsorption ability for Cr(VI), better light absorbing quality, and efficient photoexcited charge transfer could be the significant factor for the enhanced photocatalytic activity of Bi<sub>12</sub>TiO<sub>20</sub>/RGO. Under the driving force of electrostatic attraction, Cr(VI) is abundantly concentrated on the surface of the Bi<sub>12</sub>TiO<sub>20</sub>/RGO polyhedral microstructure and adsorbed on the surface of catalyst particles. It is well known that the photocatalytic reduction of Cr(VI) is a heterogeneous reaction, and the enrichment of Cr(VI) onto the photocatalyst has a great influence on the photocatalytic performance improvement. Moreover, according to the result of UV-vis spectra, the introduction of RGO could improve the utilization of visible light, and a better absorption quality is beneficial to the development of photocatalytic activities. The photoelectrons and hole separation are also critical factors. The mechanism of Cr(VI) reduction in the Bi<sub>12</sub>TiO<sub>20</sub>/RGO system is shown in Figure 9. Under visible light irradiation, photoexcited electrons in the valence band of Bi<sub>12</sub>TiO<sub>20</sub> may transfer to the conduction band due to the internal electric field. RGO is a great electron acceptor to reserve photoexcited electrons [34,35]. It hinders the recombination of photoexcited charges and prolongs their lifetime. The transferring electrons reserved on the RGO also could be trapped by Cr(VI) ions adsorbed on the surface of Bi<sub>12</sub>TiO<sub>20</sub>/RGO, and thus the Cr(VI) is reduced to Cr(III). The photogenerated holes may react with the adsorbed water on the

surface to form oxygen and hydrogen ions. It may also be oxidized to hydroxyl radicals  $\bullet\text{OH}$  [36,37], which could oxidize Cr(III) backward to Cr(VI), and the photocatalytic reduction of Cr(VI) efficiency of the photocatalyst could be suppressed. With the addition of p-hydroxybenzoic acid, photogenerated holes could be trapped by p-hydroxybenzoic acid and considerably promote the charge separation, resulting in the improved photocatalytic reduction of Cr(VI) on the surface of  $\text{Bi}_{12}\text{TiO}_{20}/\text{RGO}$ . However, with the addition of chloroacetic acid and citric acid, the Cr(VI) photocatalytic reduction is not expected to be promoted. The competitive adsorption of chloroacetic acid and citric acid with Cr(VI) might be the dominant reason for this result. Many activity sites at catalysts were occupied by the organic acid, and photoexcited electrons could also be adsorbed hunted by  $\text{O}_2$  to form  $\text{O}_2^{\bullet-}$  radicals, so the charge separation effect of the organic acids (chloroacetic acid and citric acid) did not obviously result in promoting Cr(VI) photocatalytic reduction, and even depressed the Cr(VI) reduction.

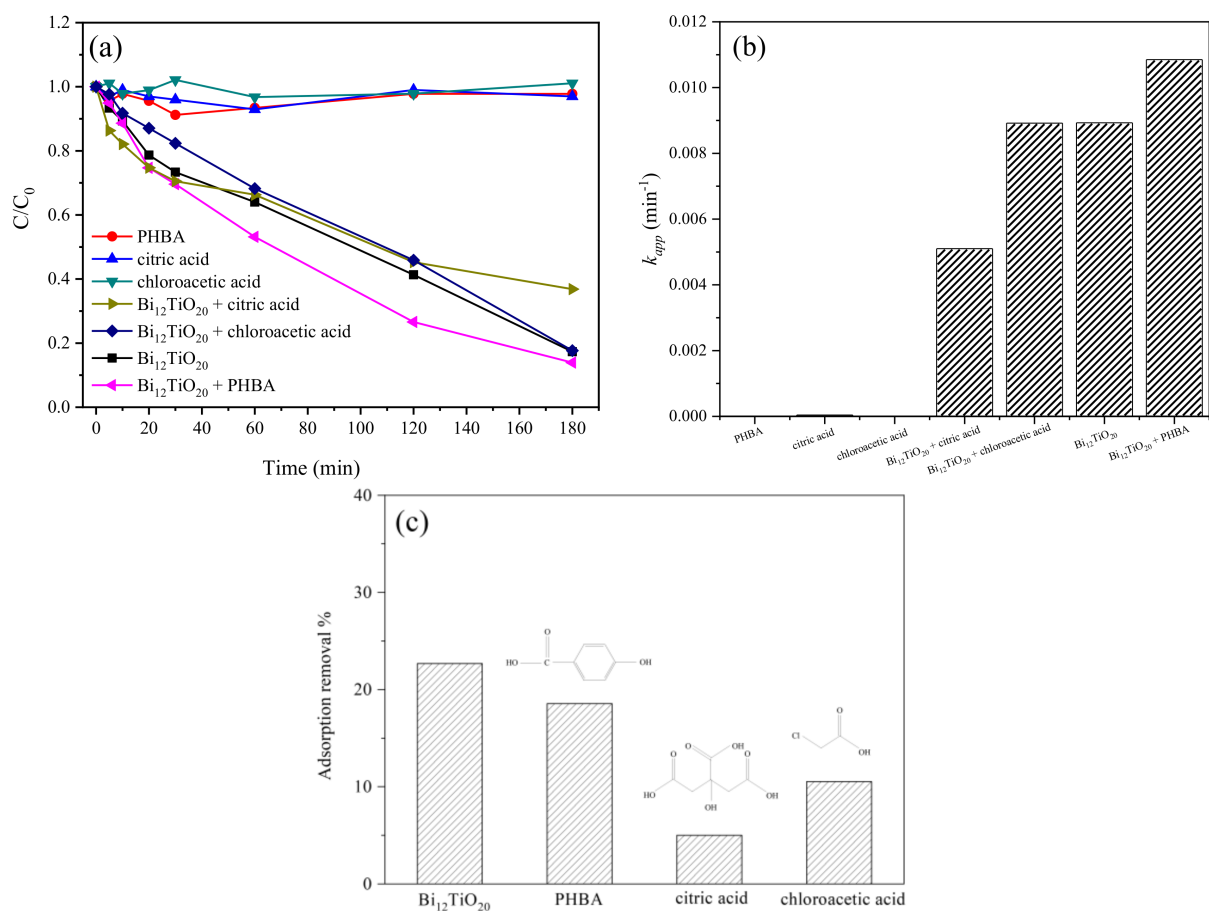


**Figure 8.** (a)  $C/C_0$  vs. time plot and (b)  $k_{app}$  for the photocatalytic reduction of Cr(VI) by  $\text{Bi}_{12}\text{TiO}_{20}/\text{RGO}$  with the addition of PHBA, chloroacetic acid, and citric acid, respectively; (c) The adsorption removal of Cr(VI) by the  $\text{Bi}_{12}\text{TiO}_{20}/\text{RGO}$  with PHBA, chloroacetic acid, and citric acid, respectively.

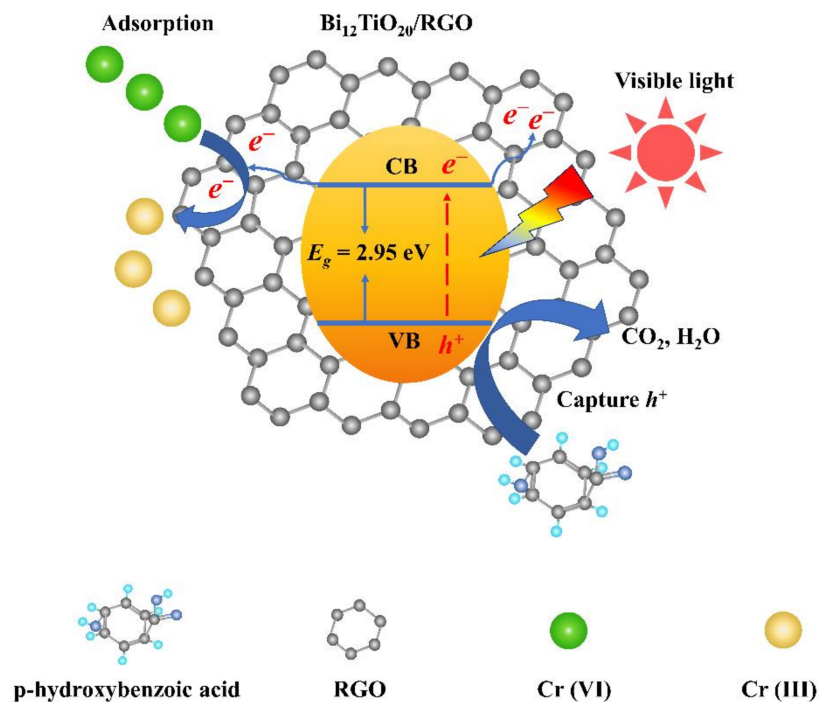


**Figure 9.** Mechanism of photocatalytic reduction of Cr (VI) in  $\text{Bi}_{12}\text{TiO}_{20}$ /RGO organic acid system.

#### 4. Conclusions

A  $\text{Bi}_{12}\text{TiO}_{20}$ /RGO polyhedral microstructure was synthesized using a simple one-step hydrothermal process. The RGO nanostructures were introduced to the  $\text{Bi}_{12}\text{TiO}_{20}$  microstructures from the XRD and FT-IR characterization. The SEM observations indicated that reaction time and the  $\text{OH}^-$  ions concentration played an important role in the formation of  $\text{Bi}_{12}\text{TiO}_{20}$  micro-polyhedral morphology. The improved photocatalytic properties of the  $\text{Bi}_{12}\text{TiO}_{20}$ /RGO for the reduction of Cr(VI) was mainly attributed to the better photo-generated electrons transfer using RGO as a promoter. Moreover, better adsorption and enrichment of Cr(VI) onto the composite catalysts provide more active sites for the photocatalytic reaction. In the presence of organic acids, the promotion effects of the organic acids on Cr(VI) photocatalytic reduction were limited by the competitive adsorption between the organics and Cr(VI). This work verified that microstructure control was an efficient method to improve the photoreduction activity of  $\text{Bi}_{12}\text{TiO}_{20}$ -based photocatalysts. In the future, further tests will be broadened on the long-term photoreduction test of hexavalent chromium using  $\text{Bi}_{12}\text{TiO}_{20}$ -based membranes, with the aim of potential application.

**Author Contributions:** Conceptualization, H.G.; methodology, H.G.; investigation, S.P. and X.L.; writing—original draft preparation, H.G. and S.P.; writing—review and editing, S.P. and Y.H.; supervision, H.G. All authors have read and agreed to the published version of the manuscript.

**Funding:** This work was supported by the National Natural Science Foundation of China (52070103), the Zhejiang Provincial Natural Science Foundation of China (LY21E090004), the Natural Science Foundation of Ningbo (No. 202003N4135), and the General Research Project of Zhejiang Provincial Department of Education (No. Y202043966).

**Institutional Review Board Statement:** Not applicable.

**Informed Consent Statement:** Not applicable.

**Data Availability Statement:** The data is available on reasonable request from the corresponding author.

**Conflicts of Interest:** The authors declare no conflict of interest.

## References

1. Salomons, W.; Förstner, U.; Mader, P. *Heavy Metals Problems and Solutions*; Springer: Berlin/Heidelberg, Germany, 1995; p. 386.
2. Khalil, S.; Awad, A.; Elewa, Y. Antidotal impact of extra virgin olive oil against genotoxicity, cytotoxicity and immunotoxicity induced by hexavalent chromium in rat. *Int. J. Vet. Sci. Med.* **2019**, *1*, 65–73. [[CrossRef](#)]
3. Luo, J.; Li, W.G.; Ye, J.G.; Zhao, Y.T.; He, G.Y.; Chen, H.Q. Preparation and characterization of Bi<sub>12</sub>TiO<sub>20</sub>/RGO as high-efficiency photocatalysts for degradation of dye wastewater. *Diam. Relat. Mater.* **2022**, *123*, 108890–108900. [[CrossRef](#)]
4. Wang, Q.; Shi, X.D.; Xu, J.J.; Crittenden, J.C.; Liu, E.Q.; Zhang, Y.; Cong, Y.Q. Highly enhanced photocatalytic reduction of Cr (VI) on AgI/TiO<sub>2</sub> under visible light irradiation: Influence of calcination temperature. *J. Hazard. Mater.* **2016**, *307*, 213–220. [[CrossRef](#)] [[PubMed](#)]
5. Choi, Y.; Koo, M.; Bokare, A.D.; Kim, D.; Bahnemann, D.W.; Choi, W. Sequential process combination of photocatalytic oxidation and dark reduction for the removal of organic pollutants and Cr (VI) using Ag/TiO. *Environ. Sci. Technol.* **2017**, *51*, 3973–3981. [[CrossRef](#)] [[PubMed](#)]
6. Gan, H.H.; Liu, J.; Zhang, H.N.; Qian, Y.X.; Jin, H.X.; Zhang, K.F. Enhanced photocatalytic removal of hexavalent chromium and organic dye from aqueous solution by hybrid bismuth titanate Bi<sub>4</sub>Ti<sub>3</sub>O<sub>12</sub>/Bi<sub>2</sub>Ti<sub>2</sub>O. *Res. Chem. Intermed.* **2018**, *44*, 2123–2138. [[CrossRef](#)]
7. Liu, J.; Gan, H.H.; Wu, H.Z.; Zhang, X.L.; Zhang, J.; Li, L.L.; Wang, Z.L. Effect of organic substrates on the photocatalytic reduction of Cr (VI) by porous hollow Ga<sub>2</sub>O<sub>3</sub> nanoparticles. *Nanomaterials* **2018**, *8*, 263. [[CrossRef](#)]
8. Luo, L.; Dong, S.; Cui, H.; Sun, L.; Huang, T. Indium sulfide deposited MIL-53 (Fe) microrods: Efficient visible-light-driven photocatalytic reduction of hexavalent chromium. *J. Colloid Interface Sci.* **2022**, *606*, 1299–1310.
9. Thara, R.; JagadeeshBabu, P.; RubenSudhakar, D. Fabrication of visible-light assisted TiO<sub>2</sub>-WO<sub>3</sub>-PANI membrane for effective reduction of chromium (VI) in photocatalytic membrane reactor. *Environ. Technol. Innov.* **2021**, *24*, 102023–102034.
10. Liu, J.; Wu, J.; Wang, N.; Tian, F.S.; Li, J. Surface reconstruction of BiSI nanorods for superb photocatalytic Cr (VI) reduction under near-infrared light irradiation. *Chem. Eng. J.* **2022**, *435*, 135152–135162. [[CrossRef](#)]
11. Wu, N.Q.; Wang, J.; Tafen, D.N.; Wang, H.; Zheng, J.G.; Lewis, J.P.; Liu, X.G.; Leonard, S.S.; Manivannan, A. Shape-enhanced photocatalytic activity of single-crystalline anatase TiO<sub>2</sub> (101) nanobelts. *J. Am. Chem. Soc.* **2010**, *132*, 6679–6685. [[CrossRef](#)]
12. Liu, G.; Yu, J.C.; Lu, G.Q.; Cheng, H.M. Crystal facet engineering of semiconductor photocatalysts: Motivations, advances and unique properties. *Chem. Comm.* **2011**, *47*, 6763–6783. [[CrossRef](#)] [[PubMed](#)]
13. Hou, J.G.; Qu, Y.F.; Krsmanovic, D.; Ducati, C.; Eder, D.; Kumar, R.V. Solution-phase synthesis of single-crystalline Bi<sub>12</sub>TiO<sub>20</sub> nanowires with photocatalytic properties. *Chem. Comm.* **2009**, *26*, 3937–3939. [[CrossRef](#)] [[PubMed](#)]
14. Guo, W.; Yang, Y.X.; Guo, Y.N.; Jia, Y.Q.; Liu, H.B.; Guo, Y.H. Self-assembled hierarchical Bi<sub>12</sub>TiO<sub>20</sub>-graphene nanoarchitectures with excellent simulated sunlight photocatalytic activity. *Phys. Chem. Chem. Phys.* **2014**, *16*, 2705–2714. [[CrossRef](#)] [[PubMed](#)]
15. Sun, H.L.; Li, J.; Zhang, G.K.; Li, N. Microtetrahedral Bi<sub>12</sub>TiO<sub>20</sub>/g-C<sub>3</sub>N<sub>4</sub> composite with enhanced visible light photocatalytic activity toward gaseous formaldehyde degradation: Facet coupling effect and mechanism study. *J. Mol. Catal. A Chem.* **2016**, *424*, 311–322. [[CrossRef](#)]
16. Ng, Y.H.; Ikeda, S.; Matsumura, M.; Amal, R.A. Perspective on fabricating carbon-based nanomaterials by photocatalysis and their applications. *Energy Environ. Sci.* **2012**, *5*, 9307–9318. [[CrossRef](#)]
17. Yang, J.; Voiry, D.; Joon Ahn, S.; Kang, D.; Kim, A.Y.; Chhowalla, M.; Shin, H.S. Two-dimensional hybrid nanosheets of tungsten disulfide and reduced graphene oxide as catalysts for enhanced hydrogen evolution. *Angew. Chem. Int. Ed.* **2013**, *52*, 13751–13754. [[CrossRef](#)]
18. Gupta, S.; Subramanian, V. Encapsulating Bi<sub>2</sub>Ti<sub>2</sub>O<sub>7</sub> (BTO) with reduced graphene oxide (RGO): An effective strategy to enhance photocatalytic and photoelectrocatalytic activity of BTO. *ACS Appl. Mater. Interfaces* **2014**, *6*, 18597–18608. [[CrossRef](#)] [[PubMed](#)]
19. Ye, M.; Chen, C.; Zhang, N.; Wen, X.; Guo, W.; Lin, C. Quantum-dot sensitized solar cells employing hierarchical Cu<sub>2</sub>S microspheres wrapped by reduced graphene oxide nanosheets as effective counter electrodes. *Adv. Energy Mater.* **2014**, *4*, 1079–1098. [[CrossRef](#)]
20. Fu, Y.S.; Chen, H.Q.; Sun, X.Q.; Wang, X. Combination of cobalt ferrite and graphene: High-performance and recyclable visible-light photocatalysis. *Appl. Catal. B-Environ.* **2012**, *111*, 280–287. [[CrossRef](#)]
21. Liu, H.X.; Mei, H.; Miao, N.X.; Pan, L.K.; Jin, Z.P.; Zhu, G.Q.; Gao, J.Z.; Wang, J.J.; Cheng, L.F. Synergistic photocatalytic NO removal of oxygen vacancies and metallic bismuth on Bi<sub>12</sub>TiO<sub>20</sub> nanofibers under visible light irradiation. *Chem. Eng. J.* **2021**, *414*, 128748–128759. [[CrossRef](#)]
22. Mihailova, B.; Bogachev, G.; Marinova, V.; Konstantinov, L. Raman spectroscopy study of sillenites. II. Effect of doping on Raman spectra of Bi<sub>12</sub>TiO<sub>20</sub>. *J. Phys. Chem. Solids* **1999**, *60*, 1829–1834. [[CrossRef](#)]
23. Zhou, J.K.; Zou, Z.G.; Ray, A.K.; Zhao, X.S. Preparation and characterization of polycrystalline bismuth titanate Bi<sub>12</sub>TiO<sub>20</sub> and its photocatalytic properties under visible light irradiation. *Ind. Eng. Chem. Res.* **2007**, *46*, 745–749. [[CrossRef](#)]
24. Zhang, Z.; Hua, Z.; Lang, J.H.; Song, Y.X.; Zhang, Q.; Han, Q.; Fan, H.G.; Gao, M.; Li, X.Y.; Yang, J.H. Eco-friendly nanostructured Zn-Al layered double hydroxide photocatalysts with enhanced photocatalytic activity. *Chem. Eng. J.* **2012**, *184*, 4607–4619. [[CrossRef](#)]
25. Jorio, A.; Filho, A.G.S. Raman studies of carbon nanostructures. *Ann. Rev. Mater. Res.* **2016**, *6*, 357–382. [[CrossRef](#)]
26. Devi, A.P.; Padhi, D.K.; Mishra, P.M. Bio-surfactant assisted room temperature synthesis of cubic Ag/RGO nanocomposite for enhanced photoreduction of Cr (VI) and antibacterial activity. *J. Environ. Chem. Eng.* **2021**, *9*, 104778–104790. [[CrossRef](#)]

27. He, G.Y.; Qian, M.G.; Sun, X.Q.; Chen, Q.; Wang, X.; Chen, H.Q. Graphene sheets-based Ag@Ag<sub>3</sub>PO<sub>4</sub> heterostructure for enhanced photocatalytic activity and stability under visible light. *Power Technol.* **2013**, *246*, 278–283. [[CrossRef](#)]
28. Chang, Y.; Zeng, H.C. Controlled synthesis and self-assembly of single-crystalline CuO nanorods and nanoribbons. *Cryst. Growth Des.* **2004**, *4*, 397–402. [[CrossRef](#)]
29. Jiang, Q.J.; Gan, H.H.; Huang, Y.; Lu, D.N.; Zhang, W.K. Peroxymonosulfate activation on carbon nano-onions modified graphitic carbon nitride via light-tuning radical and nonradical pathways. *J. Environ. Chem. Eng.* **2021**, *9*, 106592–106606. [[CrossRef](#)]
30. Shen, X.F.; Yang, Y.; Song, B.T.; Chen, F.; Xue, Q.Q.; Shan, S.D.; Li, S.J. Magnetically recyclable and remarkably efficient visible-light-driven photocatalytic hexavalent chromium removal based on plasmonic biochar/bismuth/ferroferic oxide heterojunction. *J. Colloid Interface Sci.* **2021**, *590*, 424–435. [[CrossRef](#)]
31. Li, M.Y.; Li, C.Q.; Jiang, J.J.; Zhao, Z.Q.; Dong, S.S. In Situ preparation of BiOCl<sub>0.75</sub>I<sub>0.25</sub>/g-C<sub>3</sub>N<sub>4</sub>-Cl in reduced graphene hydrogel photoanode for simultaneous removal of tetracycline hydrochloride and hexavalent chromium with efficient electricity generation. *Environ. Res.* **2022**, *212*, 113247–113252. [[CrossRef](#)]
32. Wang, L.M.; Wang, N.; Zhu, L.H.; Yu, H.W.; Tang, H.Q. Photocatalytic reduction of Cr (VI) over different TiO<sub>2</sub> photocatalysts and the effects of dissolved organic species. *J. Hazard. Mater.* **2008**, *152*, 93–99. [[CrossRef](#)] [[PubMed](#)]
33. Wrobel, K.; Corrales Escobosa, A.R.; Gonzalez Ibarra, A.A.; Mendez, G.M.; Yanez, B.E.; Wrobel, K. Mechanistic insight into chromium (VI) reduction by oxalic acid in the presence of manganese (II). *J. Hazard. Mater.* **2015**, *300*, 144–152. [[CrossRef](#)]
34. Wang, Y.Y.; Su, Y.; Fang, W.J.; Zhang, Y.C.; Li, X.C.; Zhang, G.S.; Sun, W.H. SnO<sub>2</sub>/SnS<sub>2</sub> nanocomposite anchored on nitrogen-doped RGO for improved photocatalytic reduction of aqueous Cr (VI). *Powder Technol.* **2020**, *363*, 337–348. [[CrossRef](#)]
35. Liu, C.C.; Wang, P.F.; Qiao, Y.H.; Zhou, G. Self-assembled Bi<sub>2</sub>SeO<sub>5</sub>/rGO/MIL-88A Z-scheme heterojunction boosting carrier separation for simultaneous removal of Cr (VI) and chloramphenicol. *Chem. Eng. J.* **2022**, *431*, 133289–133301. [[CrossRef](#)]
36. Romero-Morán, A.; Sánchez-Salas, J.L.; Molina-Reyes, J. Influence of selected reactive oxygen species on the photocatalytic activity of TiO<sub>2</sub>/SiO<sub>2</sub> composite coatings processed at low temperature. *Appl. Catal. B Environ.* **2021**, *291*, 119685–119698. [[CrossRef](#)]
37. Ferreira, L.C.; Fernandes, J.R.; Rodríguez-Chueca, J.; Peres, J.A.; Lucas, M.S.; Tavares, P.B. Photocatalytic degradation of an agro-industrial wastewater model compound using a UV LEDs system: Kinetic study. *J. Environ. Manag.* **2020**, *269*, 110740–110748. [[CrossRef](#)] [[PubMed](#)]